THE ASTROPHYSICAL JOURNAL, 336:1022–1040, 1989 January 15

TURBULENT COMPRESSIBLE CONVECTION IN A DEEP ATMOSPHERE. IV. RESULTS OF THREE-DIMENSIONAL COMPUTATIONS

KWING L. CHAN
Applied Research Corporation, Landover, Maryland

AND

S. SOFIA
Center for Solar and Space Research, Yale University
Received 1988 March 21; accepted 1988 July 1

ABSTRACT

We study the behavior of turbulent convection in deep atmospheres by numerically solving the three-dimensional Navier Stokes equations. Six cases with different energy fluxes, ratios of specific heats, and spatial resolutions were computed for contrasting and comparison. The numerical results are presented in the form of approximate formulae that describe the quantitative relationships among the mean variables, root-mean-square fluctuations, and correlations. The main results are the following: (i) The mean vertical velocity, which from time to time has been casually and incorrectly taken to be zero, turns out to be an important link between the buoyancy work and the heat flux. The mean vertical advection rates of all thermodynamical variables can be expressed in terms of the mean vertical velocity. (ii) In a region where convection is efficient, the total flux is composed of two main components: the enthalpy flux, and the flux of kinetic energy. The enthalpy flux can be roughly computed from the superadiabatic gradient, and vice versa. The flux of kinetic energy points downward in most of the convection zone, and its magnitude can reach the same order as the total flux. Its size is not simply related to the atmospheric structure, but is proportional to the total flux and inversely proportional to the specific heat under constant pressure. (iii) The production and dissipation of kinetic energy behave differently. The production depends mainly on the local variables and the flux, but the dissipation is nonlocal. A substantial amount of kinetic energy is carried away from the location of production, to be dissipated in lower regions.

Subject headings: convection — stars: atmospheres — Sun: atmospheric motions — turbulence

I. INTRODUCTION

The series of papers of which this is a part studies the behavior of deep, turbulent convection relevant to solar and stellar applications by means of numerical simulations. In Papers I (Chan, Sofia, and Wolff 1982) and II (Sofia and Chan 1982) of this series, two-dimensional cases were studied. They showed that both deep stratification and realistic stellar fluids can be handled, and indication was found that the sizes of the convective cells may indeed be scaled by the pressure or density scale height, a previously unjustified assumption of the mixing length theory (MLT). In Paper III (Chan and Sofia 1986) of this series, we started to study three-dimensional cases. We tested our numerical approach by varying the numerical technique, the grid resolution, the size of the domain, and the viscosity. This exercise, in addition to increasing our confidence on the method, has increased our understanding of the qualitative behavior of turbulent compressible convection. We have already discussed the general pattern of the three-dimensional (3D) convecting flows, the most prominent features being the breakup of vertical motions in scales less than the total depth of the convection zone and the long, funnel-like columns of strong downflows. We have noticed that an impenetrable side boundary tends to attract downflows, which is not a desirable effect. Since then, the numerical codes have been changed to a Cartesian configuration, and all the side boundaries have been made periodic in order to avoid such problem. Aside from the disappearance of the constant downflow near solid walls, the principal qualitative features of the flow have not changed. In this paper, we present a summary of the quantitative aspects of the results of our numerical study. However, we do not propose to follow here all the implications of the information. This will be done in subsequent papers.

For a quasi-stationary turbulent system such as a convecting atmosphere, all the statistical information is contained in the set of first-order, second-order, etc., correlation functions. If all these functions were found, the whole problem could be considered as solved. This is obviously impractical and may not even be desirable, since it would not lead to physical insights. In general, it is more beneficial to study the low-order correlations and examine their interrelations; the hope is to find closures which express certain correlation functions in terms of lower order correlations in order to avoid the infinite hierarchy of higher and higher order correlations. Along this line of thinking, the results of our numerical study of turbulent convection are presented through a list of formulae that describes the interrelations of various correlation functions.

The mixing length theory of convection obtains a closure by assuming that the velocity and the temperature fluctuation of the turbulence are simple functions of the mean structure of the atmosphere (the superadiabatic gradient) and that the flux of kinetic energy is negligible. Then the energy flux that is generated from the interior of a star can be used to determine the structure of the convective envelope. In a recent paper (Chan and Sofia 1987: hereafter CS), we have shown that the turbulence-structure relationships proposed by MLT are in approximate agreement with our numerical results. However, the assumption concerning the flux of kinetic energy turns out to be grossly incorrect.

The significant size of the flux of kinetic energy was first discussed by Massaguer and Zahn (1980) in their modal calculation of compressible convection, but the direction of this flux was uncertain because solutions with opposite flux directions were found. The predominantly downward direction of this flux was affirmed by the two-dimensional (2D) finite-difference computation of the Navier-Stokes equations performed by Hurlburt, Toomre, and Massaguer (1984). In this paper, we discuss the behavior of this flux in the light of our 3D results. While we have obtained more quantitative information, we have not been able to find a closure to handle this flux. However, our numerical results repudiate the validity of some popular closures.

In § II, we describe our numerical model and specify the parametric values of the cases computed. In § III, we discuss the behavior and relationships among the low-order (mostly second-order) correlations of the velocity and the thermodynamical variables. The relationships are expressed as analytical approximations which make the physical connections clear and can be used in future analytical work. In § IV, we discuss topics of key interests to stellar structure theory, namely, the relationships among the fluxes, the turbulence, and the structure of the convection zone. Particular attention is paid to the flux of kinetic energy. In § V, we summarize our findings and discuss necessary improvements for future computation.

II. THE NUMERICAL MODEL

The detailed description of our numerical approach has been given in Paper III. Here we only outline the most important or distinctive features. Unless otherwise stated, the symbols used here will be the same as those in that paper.

We solve the Navier-Stokes equations for an ideal gas in Cartesian coordinates (x, y, z), where z is along the vertical direction. For later reference, the equations are

$$\partial\rho/\partial t = -\nabla\cdot\rho\boldsymbol{V}, \tag{1}$$

$$\partial\rho\boldsymbol{V}/\partial t = -\nabla\cdot\rho\boldsymbol{V}\boldsymbol{V} - \nabla p + \nabla\cdot\boldsymbol{\sigma} + \rho\boldsymbol{g}\,, \tag{2}$$

$$\partial E/\partial t = -\nabla\cdot[(E+p)\boldsymbol{V} - \boldsymbol{V}\cdot\boldsymbol{\sigma} + \boldsymbol{f}] + \rho\boldsymbol{V}\cdot\boldsymbol{g}\,, \tag{3}$$

where ρ is the density, p is the pressure, $\boldsymbol{V}$ is the velocity, $\boldsymbol{g}$ is the gravitational acceleration, $E = e + (\frac{1}{2})\rho V^2$, e is the internal energy, σ is the viscous stress tensor, and $\boldsymbol{f}$ is the diffusive flux. A bold symbol denotes a vectorial (or tensorial) quantity, and a corresponding nonbold symbol denotes its scalar magnitude.

The domain of computation is a rectangular box with periodic boundaries on the four sides and impenetrable, stress-free boundaries at the top and bottom. A constant flux F_b is fed in from the bottom; at the top, the entropy is held fixed. The aspect ratio (width/depth) of the box is 1.5.

The viscosity is computed by a sub–grid-scale tubulence (SGST) viscosity formula, as discussed in Paper III; the adjustable coefficient c_μ for this viscosity is fixed at 0.20. The diffusive flux of thermal energy carried by the SGST is assumed to be proportional to the gradient of the entropy, and the Prandtl number is taken to be $\frac{1}{3}$. The initial distribution of the gas is polytropic and slightly superadiabatic (polytropic index $= 0.99\gamma/[\gamma - 1]$, where γ is the ratio of specific heats). The vertical grid spacing is roughly in scale with the local pressure scale height, and the horizontal grid is uniform. Second-order spatial accuracy is maintained through center differencing of the differential equations in strong conservation form.

TABLE 1

CHARACTERISTICS OF THE COMPUTED CASES

Case	γ	F_b	Depth	Grid
A.....	5/3	0.125	5.0	20 × 20 × 37
B.....	20/17	0.125	5.7	20 × 20 × 37
C.....	20/17	0.125	4.7	20 × 20 × 46
D.....	20/17	0.333	4.3	20 × 20 × 46
E.....	5/3	0.250	4.5	28 × 28 × 46
F.....	5/3	0.125	4.8	28 × 28 × 46

For convenience, all the quantities are made dimensionless hereafter. The scalings are chosen to make the total depth of the domain and the initial values of the density, temperature, and pressure at the top equal to 1.

The evolution of the fluid is first computed by the ADISM method which can take large time steps and saves computer time for relaxing the convecting fluid to self-consistent thermal equilibrium (see Paper III). After the flow reaches a statistically equilibrium state, which is usually indicated by a balance of the input energy from the bottom and the outgoing energy from the top (to within 1% for cases A–E, and 2.2% for case F), the calculation is switched to an Adams-Bashforth type method which gives much better time accuracy. After a few more turnover times, statistical averages are taken for the quantities of interest. The period of averaging exceeds 10 turnover times. For an arbitrary quantity q, $\langle q\rangle$ denotes its combined horizontal and temporal mean, q' denotes the deviation from the mean, and q'' denotes the root mean square (rms) fluctuation from the mean. The correlation coefficient of two quantities q_1 and q_2 is expressed as $C[q_1, q_2]$.

Six cases have been computed and their characteristics are specified in Table 1. The first column gives the case identifier; the second column gives the ratio of specific heats (γ); the third column gives the input flux (F_b); the fourth column gives the depth of the thermally relaxed fluid in pressure scale heights; and the fifth column gives the number of grids (horizontal times horizontal times vertical). Cases with different gas properties, fluxes, and resolutions are considered for comparison, and they are roughly ordered with increasing number of grid points.

III. BEHAVIOR AND RELATIONSHIPS AMONG THE FLUCTUATING VARIABLES

In this section, we discuss the interrelations of V_x, V_y, V_z, ρ', p', T', and S', where V_x and V_y are the two horizontal velocities, V_z is the vertical velocity, T is the temperature, and S is the entropy. We shall concentrate our attention on the mid-region of the convection zone, one pressure scale height away from the upper and lower boundaries, so that the ideal behavior of deep convection can be studied with little influence from these boundaries.

A summary of the numerical results in the form of approximate relations is given in Table 2. Before discussing individual relations, we describe how this table is organized. The first column of the table provides the identifier for the relation. The second column shows the relation. For an arbitrary formula of the form $q_1 = c_r q_2$, the numerical coefficient c_r is obtained by averaging over all the cases with the following procedure:

$$c_r = \Big\{\sum[(q_1/q_2)_A + (q_1/q_2)_B] + \sum[(q_1/q_2)_C + \cdots + (q_1/q_2)_F]\Big\}/138\,, \tag{4}$$

TABLE 2

A LIST OF APPROXIMATE RELATIONSHIPS OBTAINED FROM THE NUMERICAL RESULTS

Identifier	Approximation	Standard Deviation
R1	V''_x (or V''_y) $\approx 0.61V''_z$	0.05
R2	$\rho''/\langle\rho\rangle \cong 0.89T''/\langle T\rangle$	0.04
R3	$p''/\langle p\rangle \approx 0.57T''/\langle T\rangle$	0.07
R4	$S'' \cong 0.94C_p T''/\langle T\rangle$	0.03
R5	$p''/\langle p\rangle \cong 0.26V''^2/\langle T\rangle$	0.01
R6	$p'' \approx 0.51\rho V''^2_z$	0.03
R7	$T'' \sim 0.90V''^2_z$	0.10
R8	$C[T', S'] \cong 0.99$	0.01
R9	$C[\rho', S'] \approx -0.89$	0.06
R10	$C[\rho', T'] \approx -0.82$	0.05
R11	$C[p', T'] \sim 0.49$	0.05
R12	$C[V_z, T'] \cong 0.81$	0.03
R13	$C[V_z, S'] \approx 0.81$	0.03
R14	$C[V_z, \rho'] \cong -0.74$	0.03
R15	$\langle V_z\rho'\rangle = -\langle V_z\rangle\langle\rho\rangle$	...
R16	$\langle V_z p\rangle \approx 1.24\langle V_z\rangle\langle p\rangle$	0.08
R17	$\langle V_z T'\rangle \approx 1.26\langle V_z\rangle\langle T\rangle$	0.08
R18	$\langle V_z S'\rangle \approx 1.20C_p\langle V_z\rangle$	0.08
R19	$\langle V_z\rangle \sim 0.58V''^3_z/\langle T\rangle$	0.07
R20	$F_{ep} \approx 1.25C_p\langle p\rangle\langle V_z\rangle$	0.08
R21	$F_{ep} \approx 0.72C_p\langle\rho\rangle V''^3_z$	0.06
R22	$T''/\langle T\rangle \sim 1.05\Delta\nabla + 0.0027$	0.0008[a]
R23	$V''^2_z/\langle T\rangle \sim 1.17\Delta\nabla + 0.0032$	0.0011[a]
R24	$\Delta\nabla \sim 0.9[F/(0.8C_p\langle p\rangle T^{1/2})]^{2/3} - 0.002$	0.0007[a]
R25	$\langle V_z\rho V^2\rangle \cong 1.03\langle\rho\rangle\langle V_z V^2\rangle$	0.03
R26	$\langle V_z V^2\rangle \approx 1.13\langle V^3_z\rangle$	0.05
R27	$\langle p'\nabla\cdot V\rangle \cong \langle V_z p'\rangle/H_\rho$	0.01

[a] These are standard deviations of the least-squares fits.

where the subscripts A to F identify the cases. Since cases A and B have a smaller number of grids, the first summation is over vertical grid levels ranging from 8 to 28 (counted from the bottom of the domain), and the second summation is over levels 11 to 34. With these limits, grid levels within one pressure scale height from the upper and lower boundaries are excluded. This reduces the contamination by boundary effects. In a similar fashion, one can define the standard deviation of the ratios (q_1/q_2) from the mean c_r. Such standard deviations are listed in the third column of Table 2. They do not have physical meanings, but are listed here to provide some measure of the spreads of the results from the ideal relationships. The spreads may be due to numerical truncation errors, or contamination by boundary effects, or inadequacy of the formula; no attempt is made to differentiate them here.

A rather arbitrary ranking of the goodness of fit of a relation is shown by the symbol used between the left-hand side and right-hand side of the expression. The symbol " $\cong$ " is used for cases where the relative deviation (standard deviation/c_r) is less than 5%, and the fit can be considered as good; the symbol " $\approx$ " is used if the relative deviation is between 5% and 10% and the fit is fair; the symbol " $\sim$ " is used if the relative deviation is between 10% and 15%, and the relation should be considered only as suggestive.

a) *The General Behavior of the rms Fluctuations*

Figure 1 shows two examples (cases C and F) of the distributions of the vertical and horizontal rms velocities versus ln $(\langle p\rangle/\langle p_{top}\rangle)$; p_{top} is the pressure at top of the thermally relaxed fluid. The solid and dashed curves represent cases C and F, respectively; the thick and thin curves show V''_z and V''_x, respectively. The distributions of V''_x and V''_y for the same case coincide with each other in this figure. These cases have the same F_b but different γ. Since the specific heat under constant pressure $C_p[=\gamma/(\gamma-1)]$ is smaller for larger γ, the velocities of case F (with a larger γ) are substantially larger than those of case C. At both the upper and lower boundaries, V''_z goes to zero and the horizontal velocities become large as the vertical motions are turned into horizontal motions by the rigid boundaries. In the mid-region, V''_z is larger than the horizontal velocities, and the ratio between V''_x (or V''_y) and V''_z is roughly equal to 0.6. The uniformity of this ratio holds better in the case with a smaller γ, but it is quite independent of F_b. This approximate scaling relationship between the horizontal and vertical rms velocities is represented by relation R1 in Table 2.

An example (case F) of the distributions of the relative fluctuations of the thermodynamical variables $p''/\langle p\rangle$, $\rho''/\langle\rho\rangle$, and $T''/\langle T\rangle$ are shown in Figure 2. In general, $\rho''/\langle\rho\rangle$ and $T''/\langle T\rangle$ are close to each other, but they are larger than $p''/\langle p\rangle$. The ratios $(\rho''/\langle\rho''\rangle)/(T''/\langle T\rangle)$ and $(p''/\langle p\rangle)/(T''/\langle T\rangle)$ are almost uniform for all cases, and are given by R2 and R3, respectively. Given this information, one can deduce a proportional relationship between the fluctuation of entropy and the relative fluctuation of temperature, using the following equation for an ideal gas:

$$S = C_p(\ln T - \nabla_a \ln p)\,, \tag{5}$$

where $\nabla_a(=[\partial \ln (p)/\partial \ln (T)]_a)$ is the adiabatic gradient. The fluctuation of the second term on the right-hand side of equation (5) can be neglected since $T''/\langle T\rangle$ is large compared to $\nabla_a p''/\langle p\rangle$. A more accurate expression of the relationship is given by R4 in Table 2.

The fluctuations of the thermodynamical variables are related to the turbulent velocities. A dimensional argument based on the momentum equation (2) leads to the expectation that the relative pressure fluctuation is proportional to the square of the Mach number (Gough 1969). That turns out to be a rather accurate description as shown by R5. This relation can be reexpressed as $p''/\langle p\rangle \cong 0.26\gamma M^2$, where M is the Mach number. The goodness of fit of R5 is demonstrated in Figure 3, where $p''/\langle p\rangle$ is plotted versus $V''^2/\langle T\rangle$ for all the cases, V''^2 being the sum of all components of the mean square velocities. The cases A–F are represented by the triangles, crosses, asterisks, diamonds, pluses, and squares, respectively. The same convention will be used in later figures when differentiation among cases is called for.

Given the ratio V''_x/V''_z (R1), the pressure fluctuation can be related simply to the vertical rms velocity, as shown by R6. This relationship is not as accurate as R5 because the ratio of the rms velocities is only fairly uniform. Using R3, the temperature fluctuation can also be estimated from the rms vertical velocity, as shown by R7. Figure 4 plots T'' versus V''^2_z for all the cases. Comparing this figure with the previous figure shows the difference in goodness of fit between relations ranked as $\sim$ and $\cong$. In Figure 4, the data of case A show most deviation from the ideal linear relationship. This may be due to the low spatial resolution of case A. Some quantities are more sensitive to resolution than others. For the relation R7, the resolution of case A seems to be marginally adequate.

b) *The Correlation Coefficients*

The mean values of the correlation coefficients between pairs of dynamical variables are given by relations R8–R14 in Table 2. The correlation between the temperature and entropy devi-

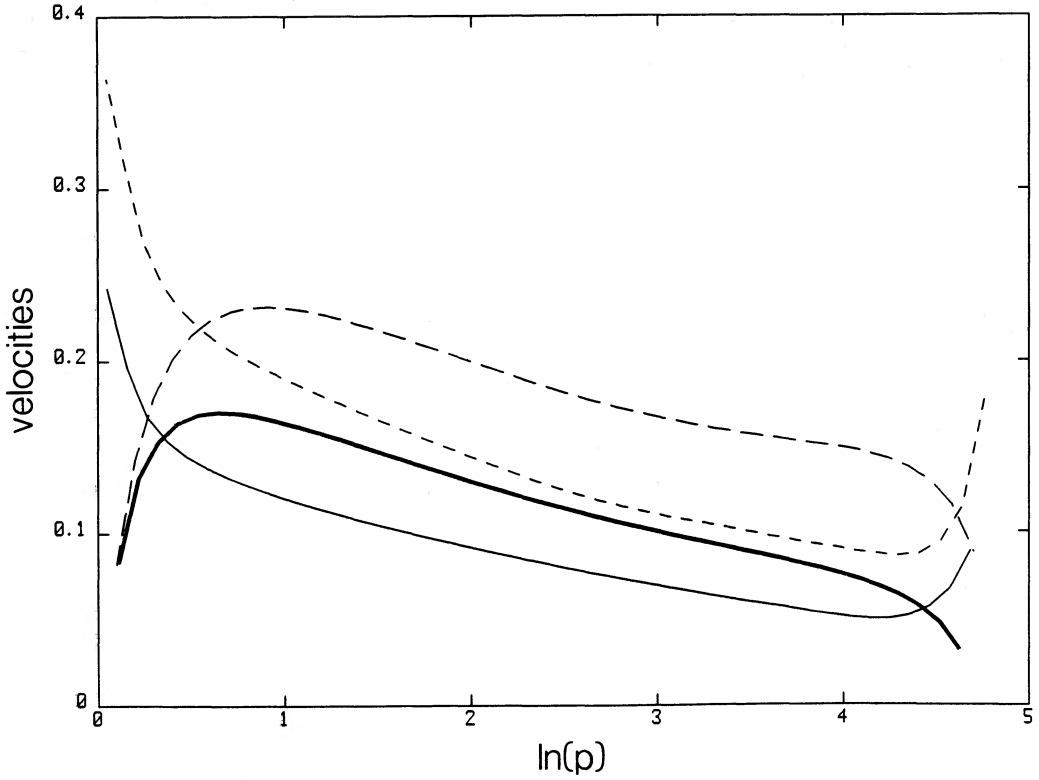

FIG. 1.—Root mean square velocities vs. depth. In this figure, like in all others, the depth is specified by ln (p/p_{top}), where p_{top} is the pressure at the top of the thermally relaxed fluid. Thick and thin solid lines show V_z'' (rms vertical velocity) and V_x'' (rms horizontal velocity) for case C; long and short dashed curves show V_z'' and V_x'' for case F, respectively.

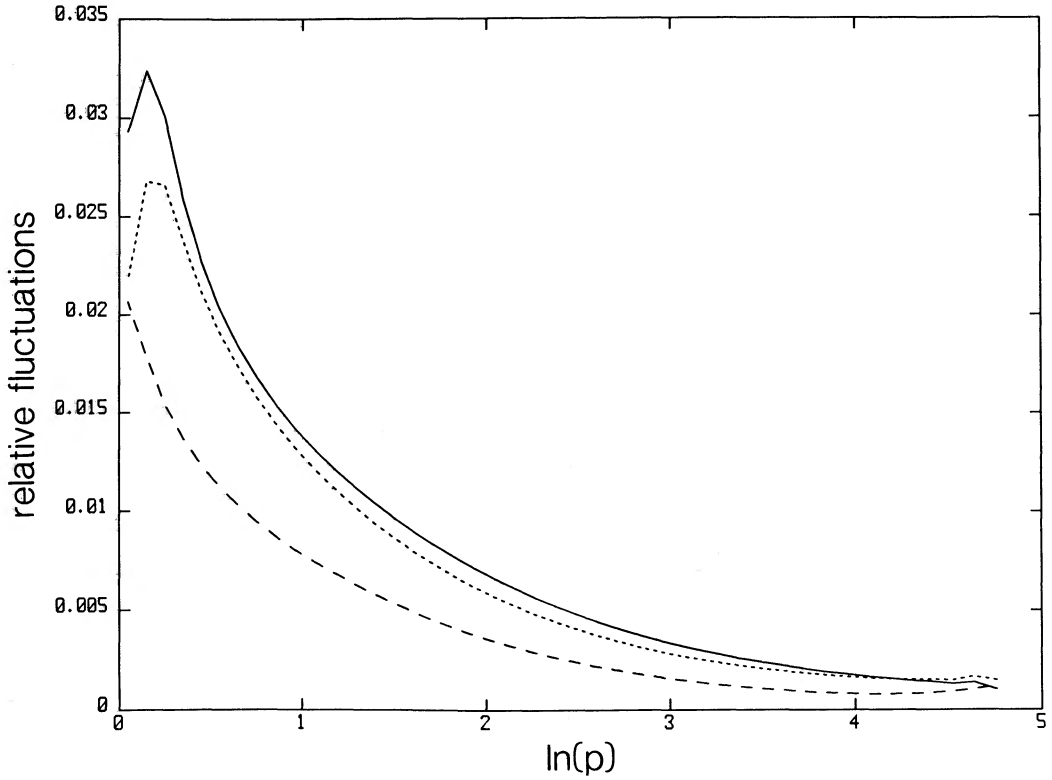

FIG. 2.—Distributions of the relative fluctuations (rms fluctuation/the mean) of the thermodynamical variables $p''/\langle p\rangle$ (*dashed curve*), $\rho''/\langle\rho\rangle$ (*dotted curve*), and $T''/\langle T\rangle$ (*solid curve*) for case F.

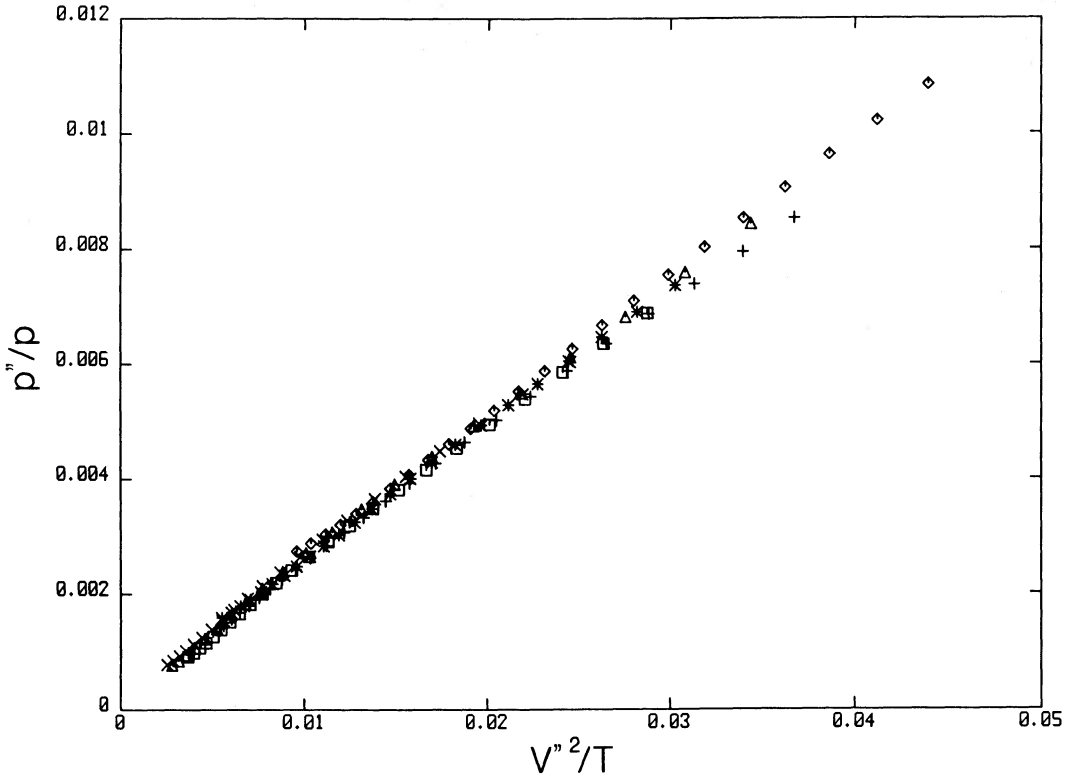

FIG. 3.—Relative pressure fluctuation $p''/\langle p\rangle$ vs. $V''^2/\langle T\rangle$ for all the cases. Cases A–F are represented by the triangles, crosses, asterisks, diamonds, pluses, and squares, respectively; this convention will also be used in later figures. The spread in the ratios between the ordinate and abscissa of all the data points is less than 5%.

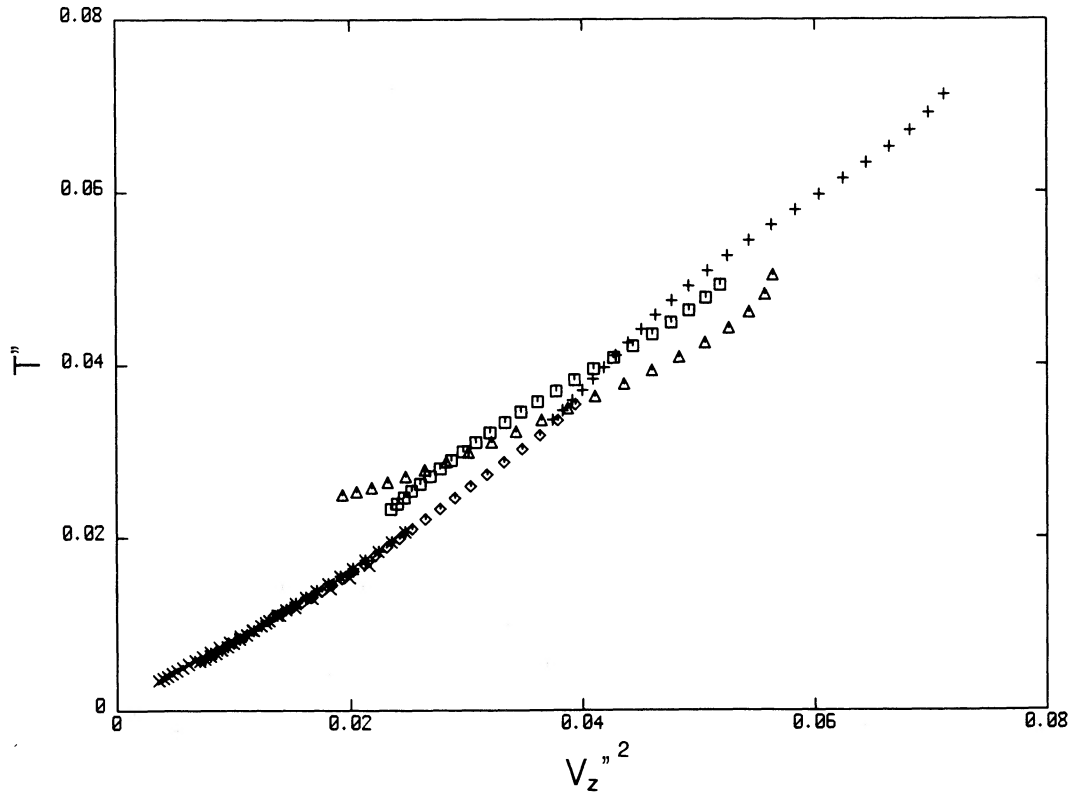

FIG. 4.—The rms temperature fluctuation T'' vs. the mean square vertical velocity $V_z''^2$ for all the cases. The spread in the ratios between the ordinate and abscissa of all the data points is 11%.

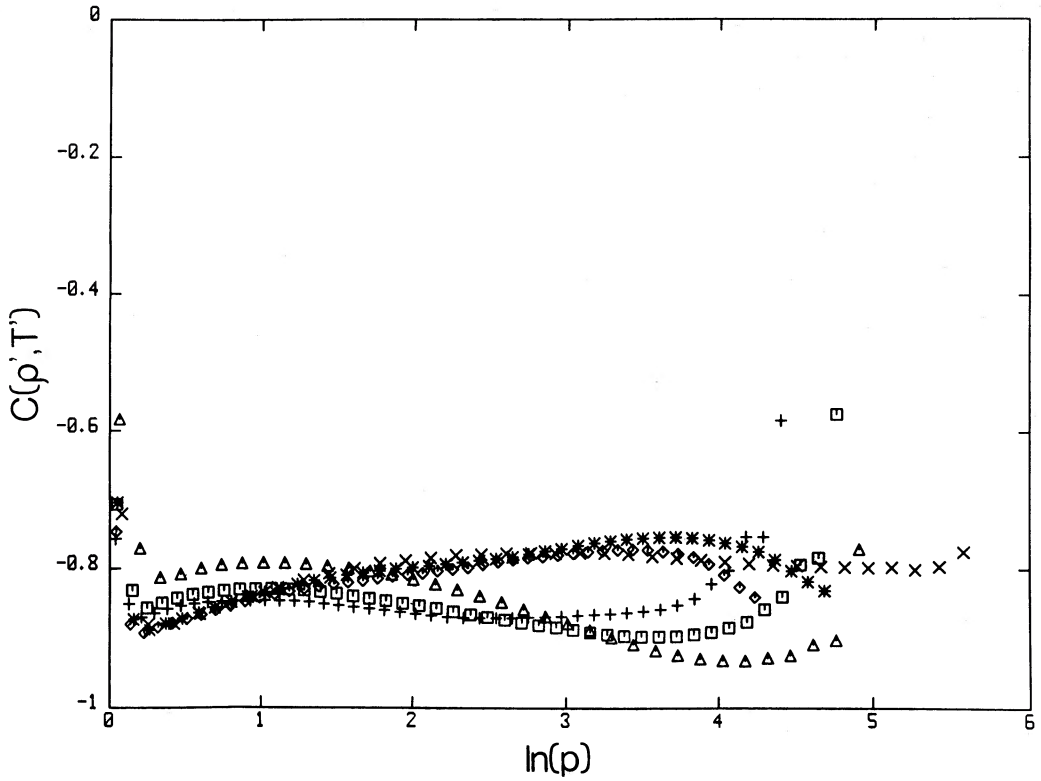

FIG. 5.—Distributions of the correlation coefficients between the density and temperature deviations, $C[\rho', T']$, for all cases. Upper boundaries all start at $\ln(\langle p\rangle/\langle p_{top}\rangle) = 0$; lower boundaries have different depths (see Table 1). The endpoints that significantly deviate from the flat distribution show boundary effects.

ations is extremely high (R8). We therefore only consider the behavior of T' here as the representative of both. The full depth distributions of the correlation coefficients $C[\rho', T]$, $C[p', T']$, $C[p', \rho']$, $C[V_z, T']$, $C[V_z, \rho']$, and $C[V_z, p']$ are shown in Figures 5–10, respectively, for all the cases.

The correlations between ρ', T', S', and V_z are generally high. In each of the Figures 5, 8, and 9, the curves show some variations over depth, but the correlation coefficient stays around some constant value close to 1 or -1. The signs of the correlations are compatible with those expected for a convecting fluid. For example, the sign of $C[V_z, \rho']$ is negative, in agreement with the expectation that lighter fluid elements go up and heavier fluid elements go down.

The correlations between p' and other variables are not as well-behaved. Figure 6 shows that $C[p', T']$ usually has low values, and the variations over depth and from case to case are substantial. The uncertainty level of R11 is high. Figures 7 and 10 show that the situation for $C[p', \rho']$ and $C[V_z, p']$ is even worse; they cannot be approximated by constant values. The effects of the impenetrable boundaries are illustrated in these figures. Near the lower boundary, $C[V_z, p']$ turns negative, showing that compression is associated with the downward moving fluid elements which run into the solid bottom; compression of the upward moving elements at the upper boundary is indicated by the positive peak of $C[V_z, p']$ at the top. For the same physical reason, $C[p', \rho']$ shows peaks near these two boundaries.

Some of the correlation coefficients can be derived from the relations among the rms fluctuations discussed in the previous subsection. For example, taking the square of the ideal gas relationship

$$p'/p \cong \rho'/\rho + T'/T\,, \tag{6}$$

and using R2 and R3, one can obtain an estimate of -0.86 for $C[\rho', T']$. It is a little different from the direct result given by R10, but is within the range enclosed by the quoted standard deviation. Similarly, one can show that $C[p', T']$ and $C[p', \rho']$ are on the order of $(p''/\langle p\rangle)/(2T''/\langle T\rangle)$, relatively small. By multiplying T' with the perturbation of equation (5) and taking averages, the very high correlation between T' and S' is also anticipated. The low correlation between p' and V_z is consistent with $C[V_z, \rho']$, $C[V_z, T']$ having opposite signs and similar absolute values.

In Paper III, streamline plots have illustrated that downflows tend to generate vortices. Quantitatively, this is shown by the correlation coefficient $C[V_z, |(\nabla \times V)_z|]$ plotted here in Figure 11 which includes all the cases. Starting with a value around -0.1, this coefficient slightly increases its magnitude and reaches about -0.2 in the middle layer; due to the compression of horizontal cross sections by the density stratification, downdrafts amplify the intensity of the vertical vorticity. Near the lower boundary, however, the vertical vorticity is amplified by the updrafts that pull neighboring fluid into smaller areas, and the correlation coefficient turns positive to about $+0.1$. Although the general behavior is similar, the distributions shown in Figure 11 do not agree quite well, even for cases with the same F_b and γ (the pairs [A, F] and [B, C]). This may be due to the sensitive dependence of the vorticity on grid resolution; cases with smaller grid spacing produce higher values of rms vorticity.

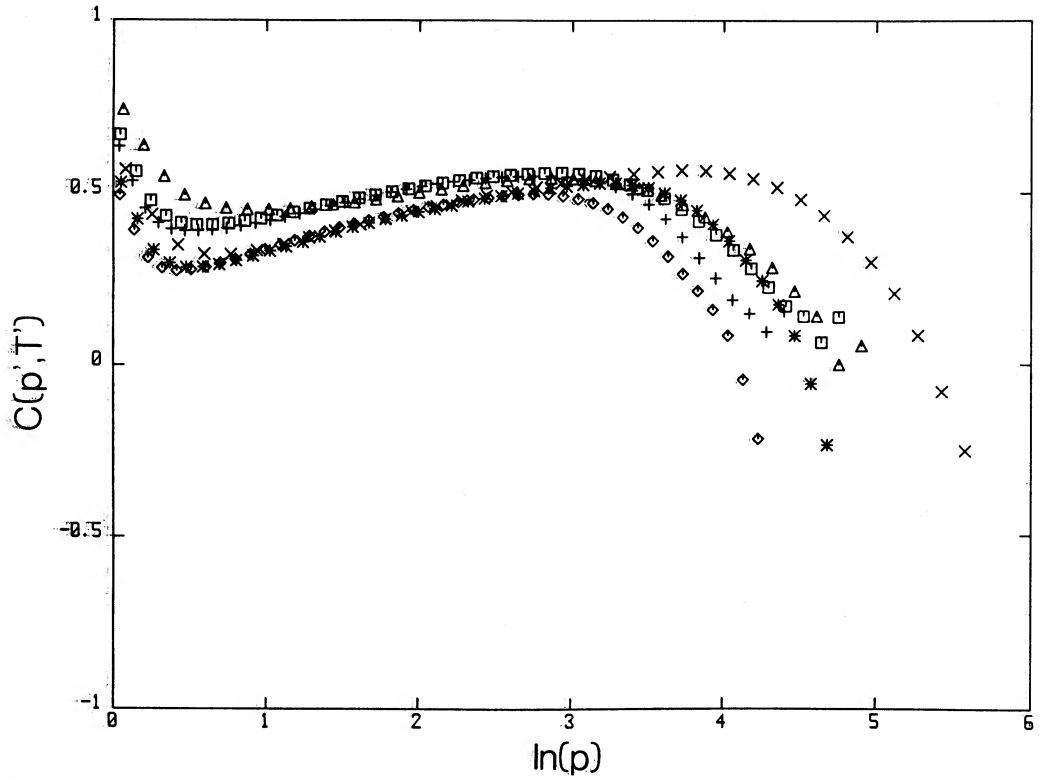

FIG. 6.—Correlation coefficient between the pressure and temperature deviations, $C[p', T']$, vs. depth for all cases. Even though the values of the correlation coefficient are not high, the pressure and temperature deviations are generally positively correlated. However, $C[p', T']$ turns negative near the lower boundary where the cooler downdrafts hit the bottom and get compressed.

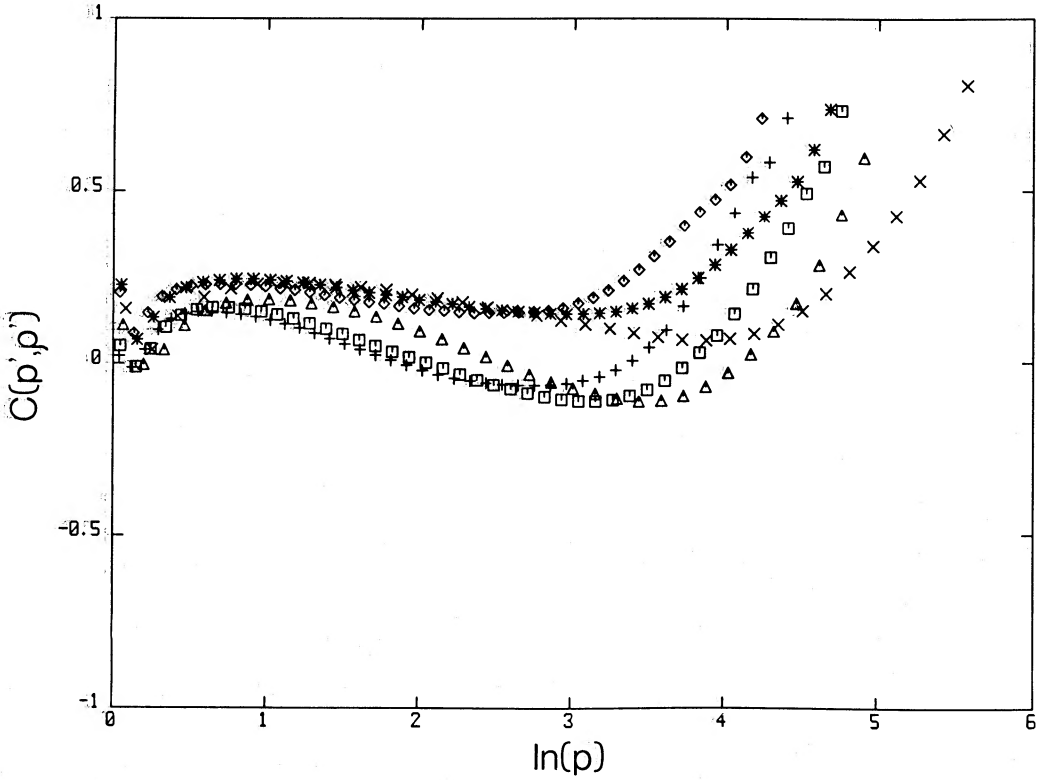

FIG. 7.—Correlation coefficient between pressure and density deviations, $C[p', \rho']$, vs. depth for all cases. The correlation is generally low, except near the lower boundary where the compression of downdrafts produces large positive values.

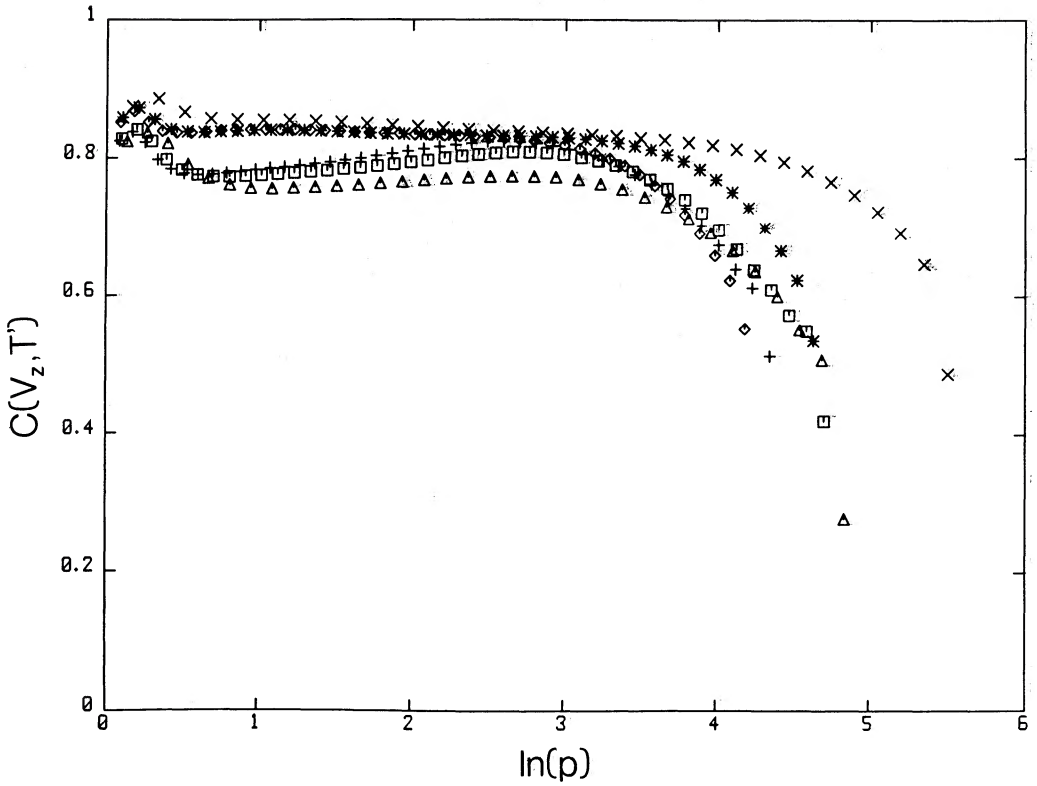

FIG. 8.—Correlation coefficient between the vertical velocity and temperature deviation, $C[V_z, T']$, vs. depth for all cases. The correlation is generally quite high and uniform; hotter fluid elements tend to move upward at all depths.

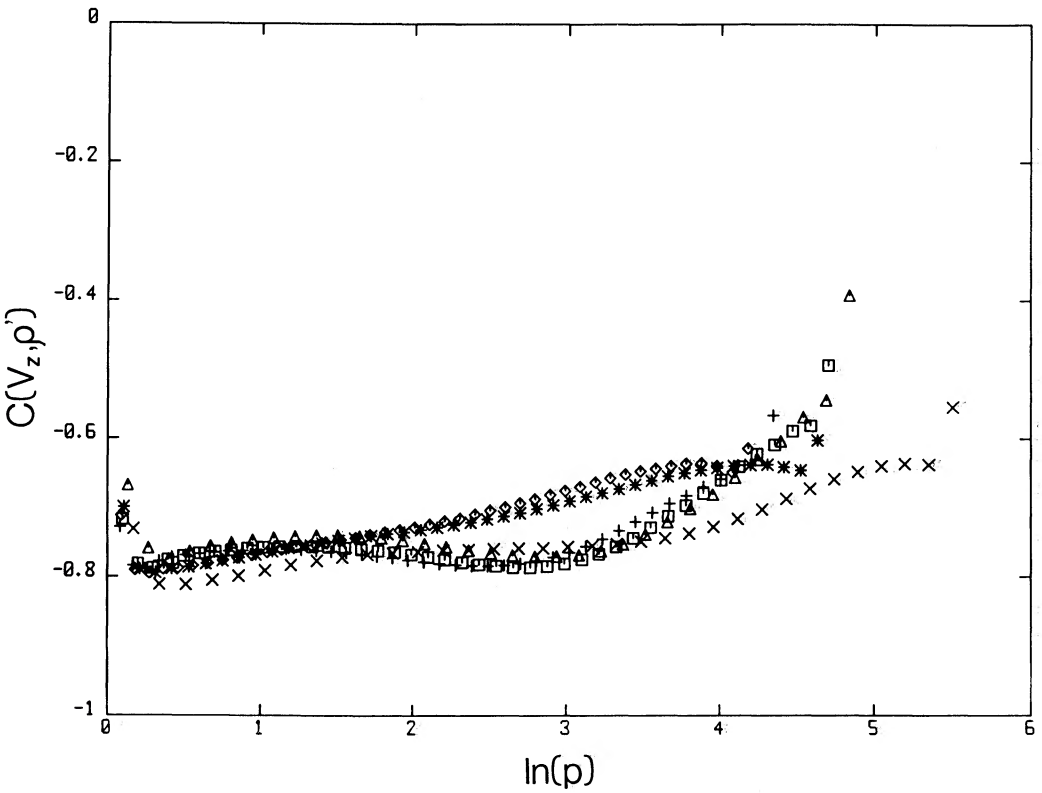

FIG. 9.—Correlation coefficient between the vertical velocity and density deviation, $C[V_z, \rho']$, vs. depth for all cases. Lighter fluid elements tend to move upward at all depths.

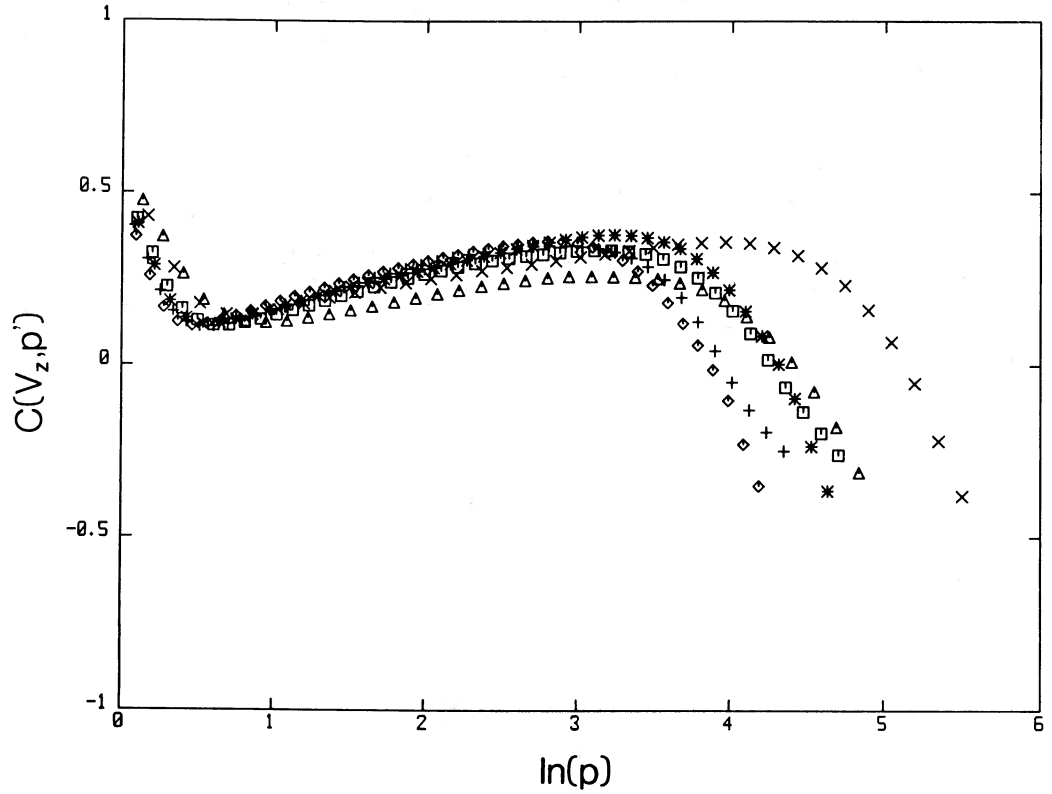

FIG. 10.—Correlation coefficient between the vertical velocity and pressure deviation, $C[V_z, p']$, vs. depth for all cases. Fluid elements with a positive pressure deviation generally tend to move upward, except near the bottom where the compression of downdrafts due to the lower boundary is again evident.

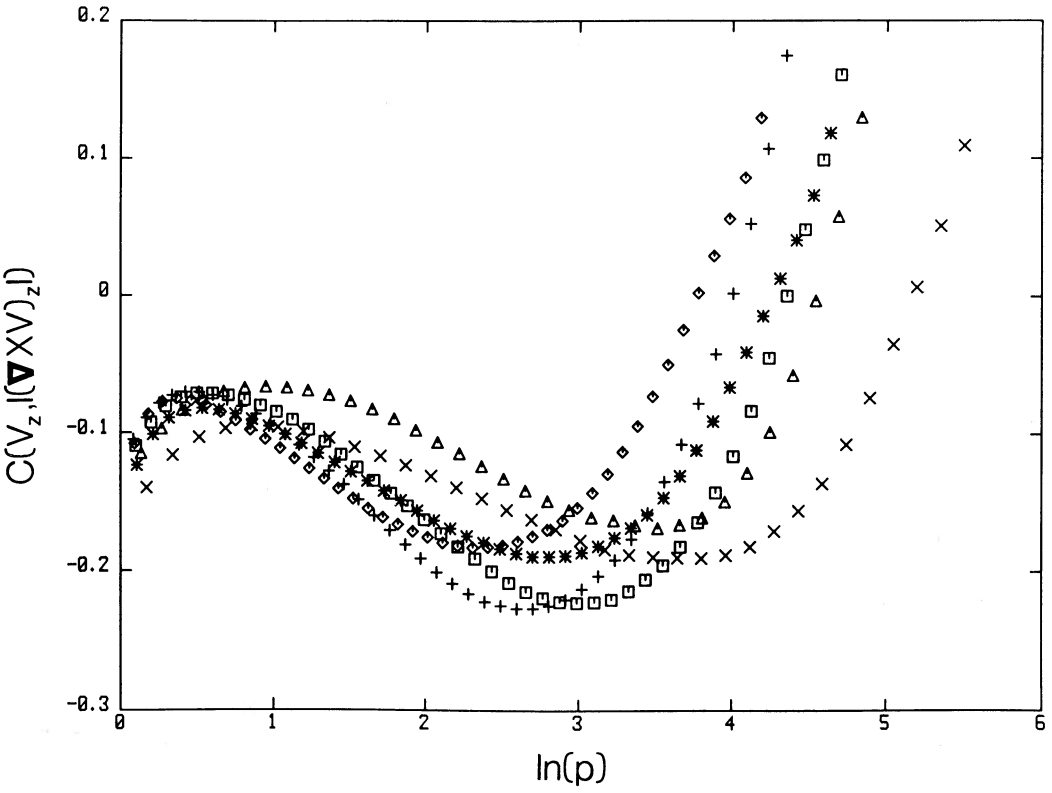

FIG. 11.—Correlation coefficient between the vertical velocity and the vertical vorticity, $C[V_z, |(\nabla \times V)_z|]$, vs. depth for all cases. Starting around a level of -0.1 at the top, this correlation grows slightly in magnitude in the middle region; the downdrafts usually amplify the vertical vorticity due to the compression of horizontal cross sections. Near the lower boundary, the vertical vorticity is amplified by the updrafts pulling the neighboring fluid into a smaller area.

c) Covariances of V_z with the Thermodynamical Variables

These covariance functions describe the mean vertical advection of the thermal quantities and are important for estimating the buoyancy work and the heat flux to be discussed in the next section. A list of relations that reduce these functions to lower order means are given by R15–R18 in Table 2. Each covariance can be expressed as a product of the mean thermodynamical variable with the mean vertical velocity.

R15 is an identity derivable from the mass conservation equation (1):

$$\langle \rho V_z \rangle = 0 , \tag{7}$$

by substituting ρ with $\langle \rho \rangle + \rho'$; therefore, no estimate of standard deviation needs to be given. R16 implies that $\langle V_z p' \rangle$ is small compared to $\langle V_z \langle p \rangle \rangle$. Given R16, the relation R17 can be derived by replacing ρ with $(p/\langle T \rangle)(1 - T'/\langle T \rangle)$ in equation (7). Figure 12 plots $\langle V_z T' \rangle$ versus $\langle V_z \rangle \langle T \rangle$ to show the goodness of fit of this fair relation. Contrary to the situation with pressure, R17 shows that one cannot make the approximation $\langle V_z(\langle T \rangle + T') \rangle \sim \langle V_z \rangle \langle T \rangle$ by arguing that T' is much smaller than $\langle T \rangle$. The relation R18 can be derived from R17 through equation (5).

Using relations R7, R12, and R17, the mean vertical velocity can be roughly related to the rms vertical velocity as shown by R19.

IV. THE FLUXES

The mean of the terms inside the divergence of the energy equation (3) can be expressed as a sum of four vertical fluxes:

$$F = F_{ep} + F_k + F_v + f , \tag{8}$$

where

$$F_{ep} \equiv \langle V_z(e + p) \rangle \tag{9}$$

is the enthalpy flux,

$$F_k \equiv \langle V_z(\tfrac{1}{2})\rho V^2 \rangle \tag{10}$$

is the flux of kinetic energy,

$$F_v \equiv \langle V_i \sigma_{iz} \rangle \tag{11}$$

is the viscous flux, and f is the diffusive flux. The sum of these fluxes should be equal to the total flux through the convection zone (F_b). An example (case E) that shows the distributions of these fluxes is given in Figure 13 where F, F_{ep}, F_k, F_v, and f are represented by the thick solid, solid, dashed, dotted, and dot-dashed curves, respectively. One can see immediately that F_v and f due to SGST are very small compared to the other fluxes, except near the upper and lower boundaries where the advective fluxes approach zero and the energy flow must be carried by the diffusive flux. The flux of kinetic energy, contrary to the assumptions of MLT and some other analytical theories, has large size and is pointing downward. Furthermore, its absolute magnitude increases with depth. Therefore, to make the total flux equal to the input flux, the enthalpy flux has to increase with depth. We discuss the relations of these two fluxes with the convective turbulence in detail in the following subsections.

a) The Enthalpy Flux

For an ideal gas, equation (9) can be rewritten as

$$F_{ep} = C_p \langle V_z p \rangle = C_p \langle \rho \rangle \langle V_z T' \rangle . \tag{12}$$

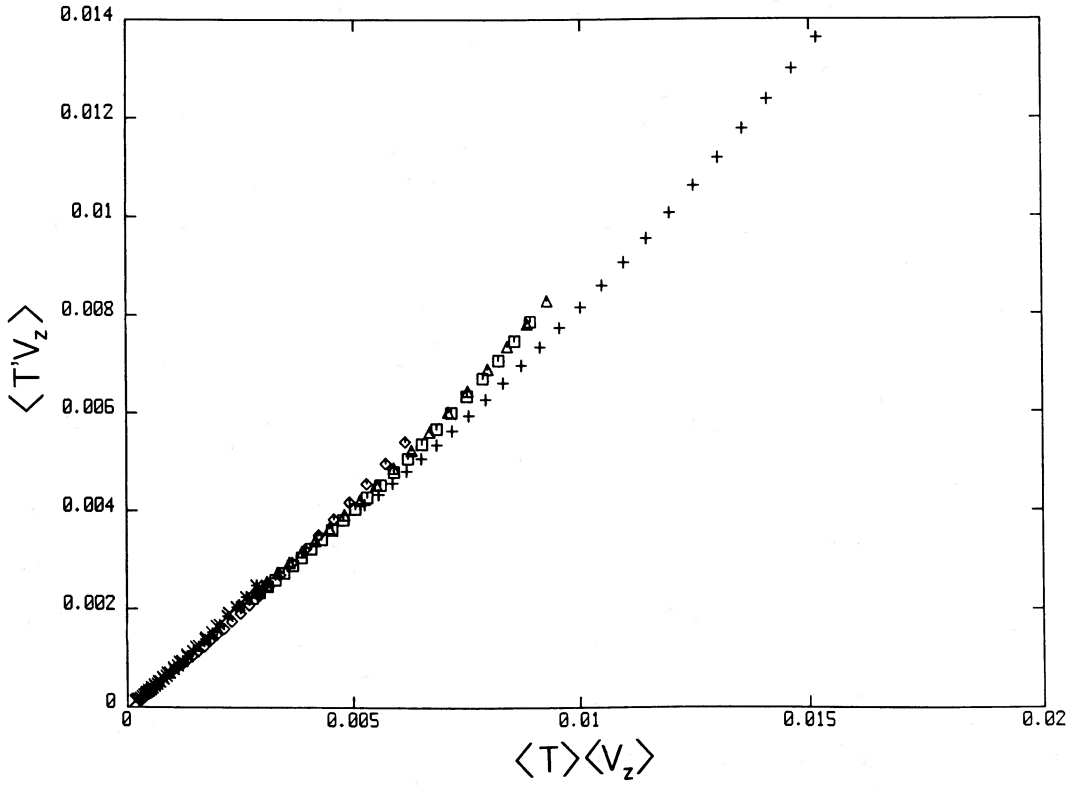

FIG. 12.—The covariance of the temperature deviation and vertical velocity vs. the product of the mean temperature and mean vertical velocity

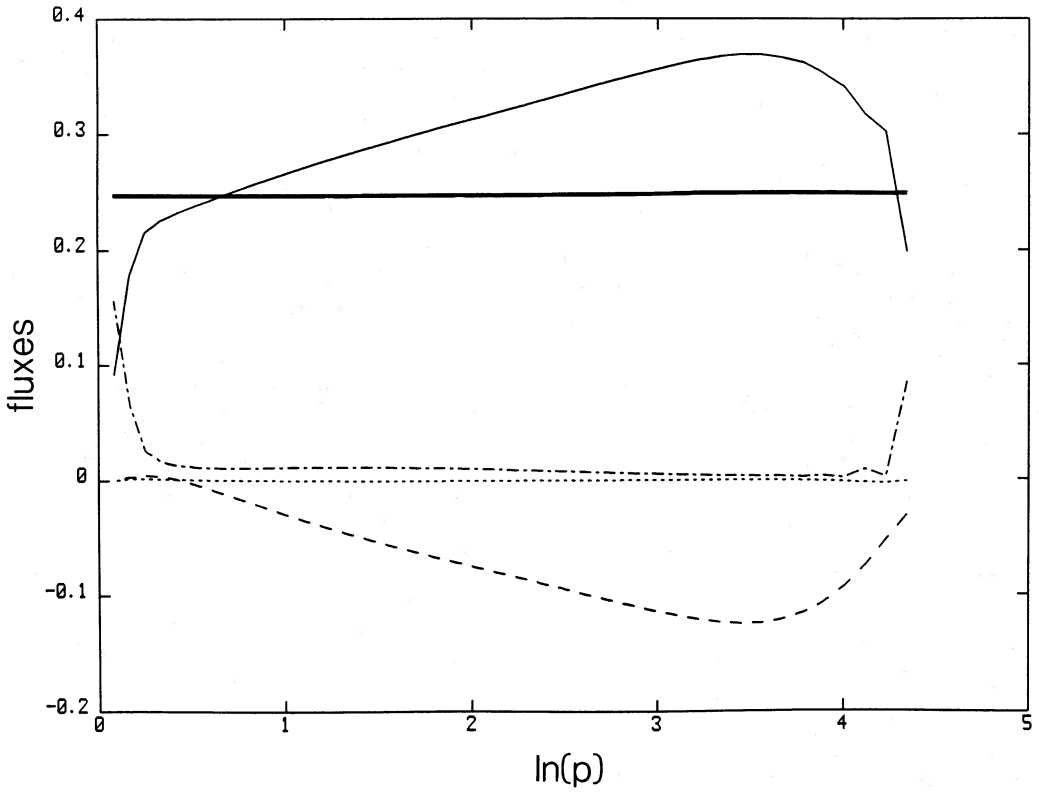

FIG. 13.—Distributions of the fluxes for case E. The thin solid, dashed, dotted, and dot-dashed curves represent F_{ep}, F_k, F_v, and f, respectively. The sum of these four fluxes is represented by the thick solid curve; it is within 1% of the input flux at all depths.

Therefore, the enthalpy flux can be related to the mean or the rms vertical velocity through R16 or R19. The results are R20 and R21, respectively.

Can one go one step further by computing $\langle V_z \rangle$ or V_z'' from the mean structure of the convection zone? If that is possible, the enthalpy flux can be completely determined from the structure of the convection zone, or vice versa. MLT has some recipes for this purpose. In CS, we discussed numerical results that indicate the validity of some of the relations proposed by MLT. The longitudinal correlation of the vertical velocity was shown to be scaled by the pressure scale height, independent of γ and F_b, and the mean square vertical velocity and temperature fluctuation are proportional to the superadiabatic gradient, $\Delta\nabla \equiv [\partial \ln (T)/\partial \ln (p)] - \nabla_a$. Here we substantiate these results further.

First, we reexamine the scaling effects of the pressure scale height by looking at the two-point vertical correlation of the temperature deviation, in a way similar to what we have done for the vertical velocity. The correlation function B is defined as

$$B = \langle T_1' T_2' \rangle / (T_1'' T_2'') , \tag{13}$$

where the subscripts 1 and 2 denote two depth levels. With one level fixed, say level 1, Figures 14*a* and 14*b* plot this function versus $\ln (p_2) - \ln (p_1)$ and $\ln (\rho_2) - \ln (\rho_1)$, respectively, for cases C, D, E, and F. The dependence of this function on $\ln (p)$ is insensitive to γ, but its dependence on $\ln (\rho)$ varies for different γ. Therefore, the vertical correlation length of temperature deviation is also scaled by the pressure scale height, not by the density scale height. Figure 15 compares the distributions of this function with level 1 fixed at two different depths (for case F). It illustrates the translational invariance of the shape of this correlation function in terms of $\ln (p)$. A similar exercise using S' instead of T' yields the same results.

The relationships between V_z'' and T'' with $\Delta\nabla$ are approximately linear, as already shown in Figures 3 and 4 of CS. The least-squares fits to these relations with data from all the studied cases are given by R22 and R23. These linear relations (also R24, to be discussed later) do not pass through the origin, since V_z'' and T'' do not vanish even when $\Delta\nabla$ is zero. The standard deviations listed for them in Table 2 are not the standard deviations of the slopes; they are the standard deviations of the numerical data from the fits.

For application to the study of stellar structures, the most important role of a convection theory is to link the total flux to the mean structure of the envelope. Using equation (12), and relations R22, R23, one can show what F_{ep} is approximately proportional to $\Delta\nabla^{2/3}$. However, that is incomplete since F_{ep} is different from F_b due to the presence of F_k. A redeeming factor is that F_k becomes significant only in the deep region of the convection zone, where $\Delta\nabla$ is very small and the flux-structure relationship is not needed as much. By inverting the functional dependence of F_{ep} on $\Delta\nabla$ and ignoring the difference between F_{ep} and F_b, we find a relationship R24 that expresses $\Delta\nabla$ in terms of F_b. The distribution of the actual numerical data is shown in Figure 16. The spread of the data is substantial, but the relative accuracy improves for large superadiabatic gradients which are more relevant to stellar structure calculations. If MLT uses proportionality constants given by Cox and Giuli (1968), a mixing length ratio of 2.3 can be inferred from relation R24.

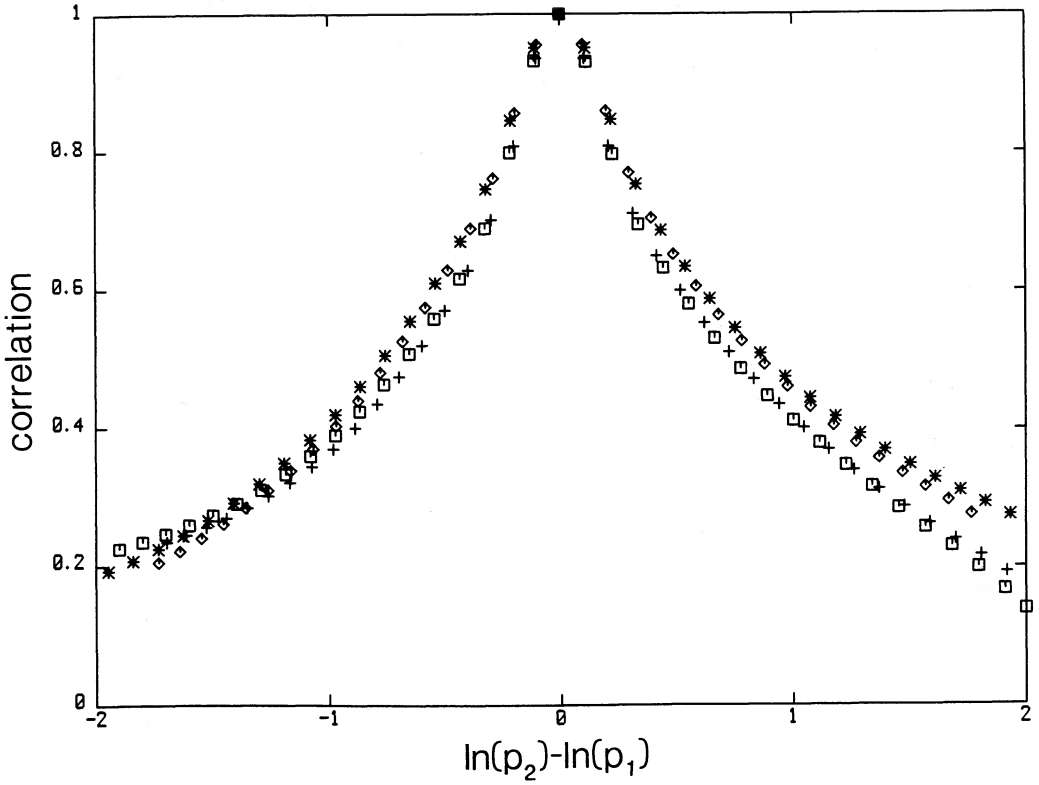

FIG. 14*a*

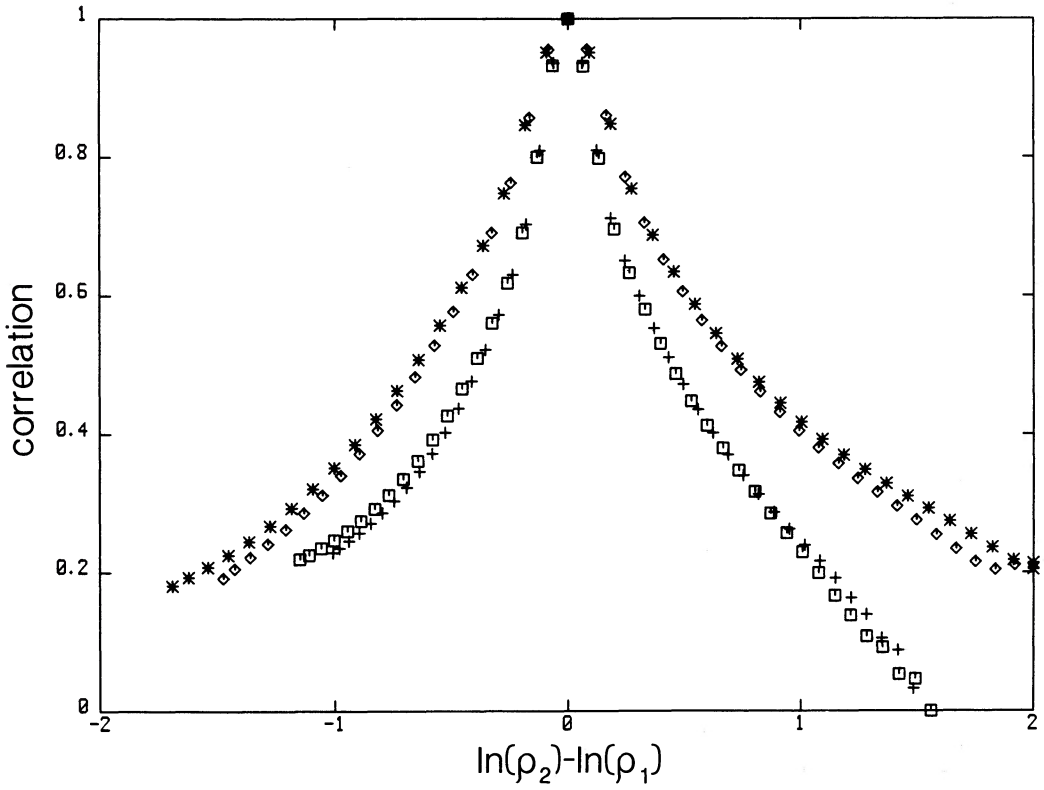

FIG. 14*b*

FIG. 14.—(*a*) Distributions of the two-point correlation function of temperature deviation $B(p_1, p_2)$ for cases C–F plotted as functions of the logarithmic pressure. All the cases coincide with each other quite well; the slight discrepancy at the right side of the figure may be caused by the difference in resolution. (*b*) Distributions of $B(p_1, p_2)$ for cases C–F plotted as functions of the logarithmic density. The distributions fall into two distinctive groups, each corresponding to a different value of γ. Thus, this correlation function is not scaled by the density scale height.

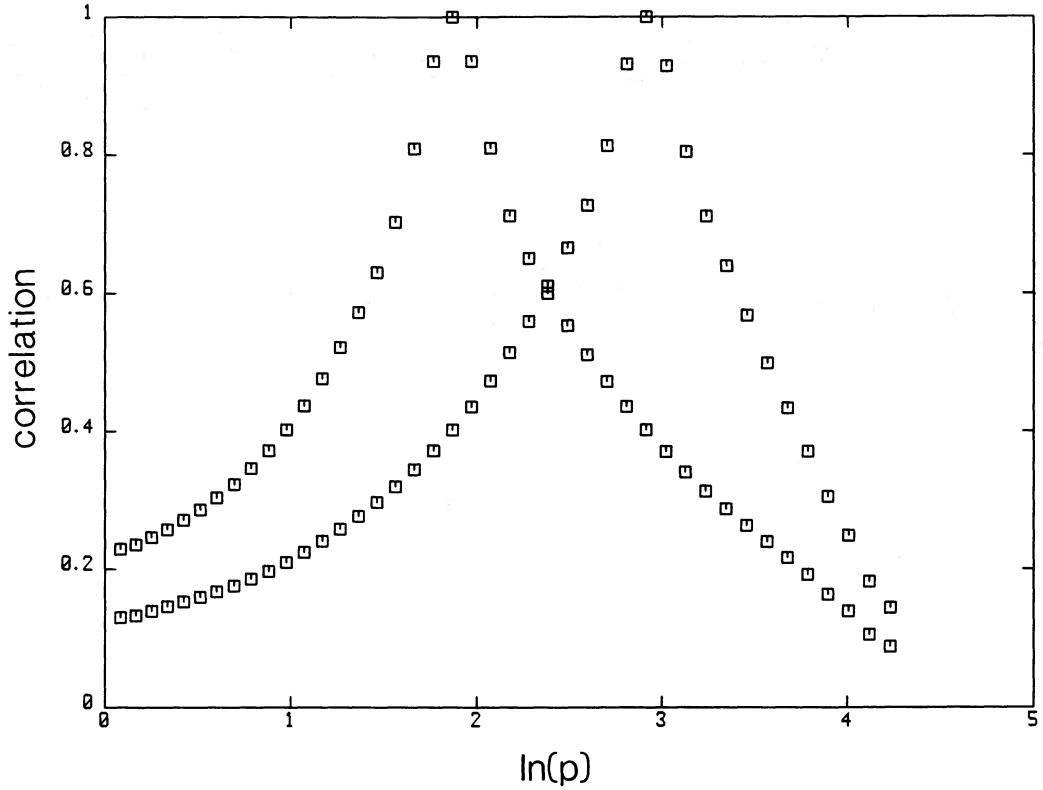

FIG. 15.—Two distributions of $B(p_1, p_2)$ for case F, with p_1 fixed at different depths (about one pressure scale height apart). The two distributions are quite symmetric and similar to each other, showing that B is a function of $|\ln(p_2) - \ln(p_1)|$.

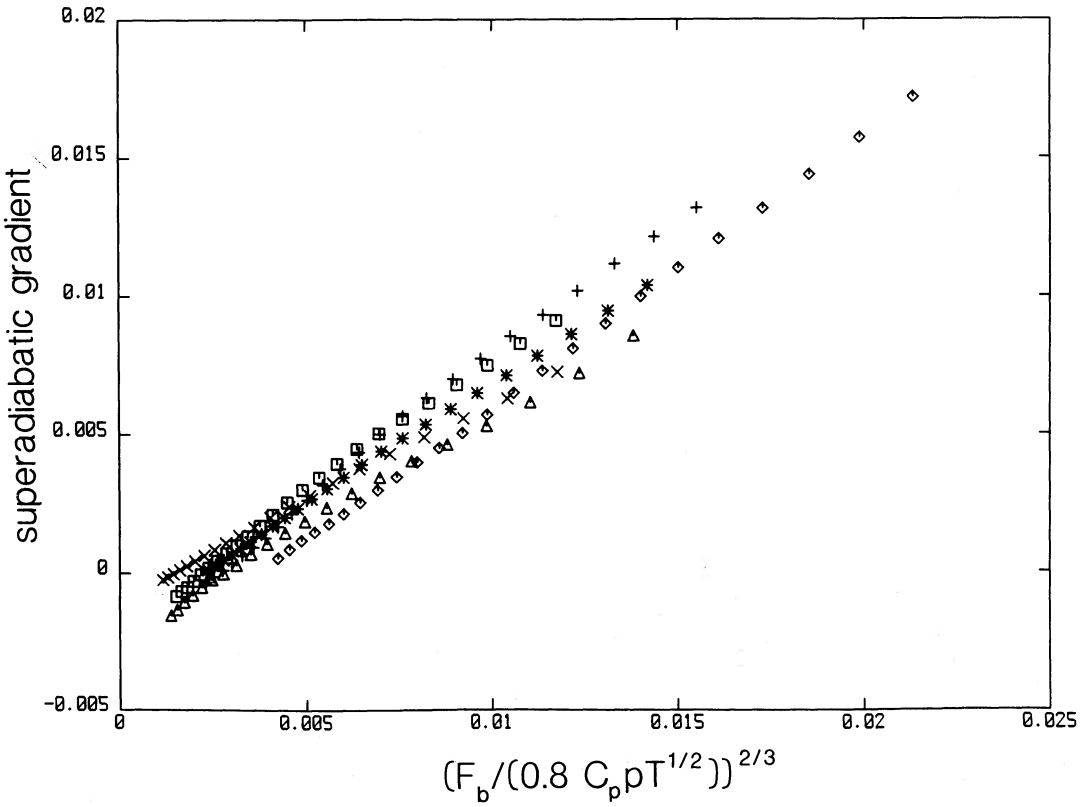

FIG. 16.—The superadiabatic gradient $\Delta\nabla$ vs. the estimate $[F_b/(0.8C_p pT^{1/2})]^{2/3}$ for all cases. While the estimate is positive definite, the superadiabatic gradient can pass through 0. This estimate is only appropriate when $\Delta\nabla$ is large, say >0.005.

b) The Flux of Kinetic Energy

From Figure 13, we can see that the description of a convection zone without the consideration of F_k is extremely incomplete. While F_{ep} is related to the superadiabatic gradient, F_k is not. In all the cases here, F_k increases with depth until it is stopped by the lower boundary. It is not clear what will be the natural development of this flux if the convection zone becomes much deeper. If its magnitude keeps on increasing, it has serious implication on overshooting into stable regions below deep stellar convection zones.

Several ways have been proposed to approximate the correlation function $\langle V_z \rho V^2 \rangle (= 2F_k)$ by lower order correlation functions. Treating the advection of kinetic energy as diffusion, one way is to approximate this correlation function by $-hV_z'' \partial \langle \rho V^2 \rangle / \partial z$, where h is some sort of mixing length. This approximation is clearly incorrect because, as shown in Figure 17 (for cases D and F), the kinetic energy increases with depth, and the negative of its gradient points upward, opposite to the prevalent direction of F_k. A simplification can be made, however, by pulling ρ out from the correlation function as shown by R25. Another step can be made by eliminating the appearance of V_x and V_y, as shown by R26. The problem is therefore reduced to finding an approximation for $\langle V_z^3 \rangle$.

In Figures 18*a* and 18*b*, we compare the approximations $V_z'' \partial V_z''^2 / \partial \ln p$ (*dotted curves*), $V_z'' \partial V_z''^2 / \partial \ln \rho$ (*dashed curves*), and $-V_z''^3$ (*pluses*) with $\langle V_z^3 \rangle$ (*solid curves*) for cases D and F, respectively. These two cases are chosen as examples with different γ. None of the approximations are satisfactory, even though the first two are able to indicate some trends (the second one encompasses both cases a little better) and the third one provides fair estimates in the lower region ($\langle V_z^3 \rangle \sim -1.1 V_z''^3$ in the region within two pressure scale heights from the bottom, including the location where $|F_k|$ is maximum).

Due to the inadequacy of simple approximations, we turn to study in detail the equation that describes the change of F_k with depth, so that further understanding of F_k can be obtained by analyzing the individual terms. The equation for kinetic energy, derived from equation (2), can be reduced to the form

$$\partial (F_k + F_v + F_{p'}) / \partial z = W_g - W_v + W_{p'} , \tag{14}$$

where

$$F_{p'} = \langle V_z p' \rangle \tag{15}$$

is the flux of pressure fluctuation,

$$W_g = -\langle V_z \rho' \rangle |g| \tag{16}$$

is the rate of buoyance work due to gravity,

$$W_v = (\tfrac{1}{2}) \langle \sigma : s \rangle , \tag{17}$$

where s is the strain rate tensor and the double dot denotes contraction to a scalar, is the rate of viscous dissipation, and

$$W_{p'} = \langle p' \nabla \cdot V \rangle \tag{18}$$

can be identified as the work rate of the pressure fluctuation.

On the left-hand side of equation (14), the viscous flux F_v can be neglected because it is very small compared to F_k (see Fig. 13*a*). The quantities $F_{p'}$ and $W_{p'}$ are related by R27 in which H_ρ is the density scale height. For the right-hand side, a comparison of the distributions of W_g, W_v, and $W_{p'}$ (for case F) is shown in Figure 19. The magnitude of $W_{p'}$ is small compared to the other work rates. At the upper region, W_g reaches a maximum and dominates over W_v. One can understand why the rate of

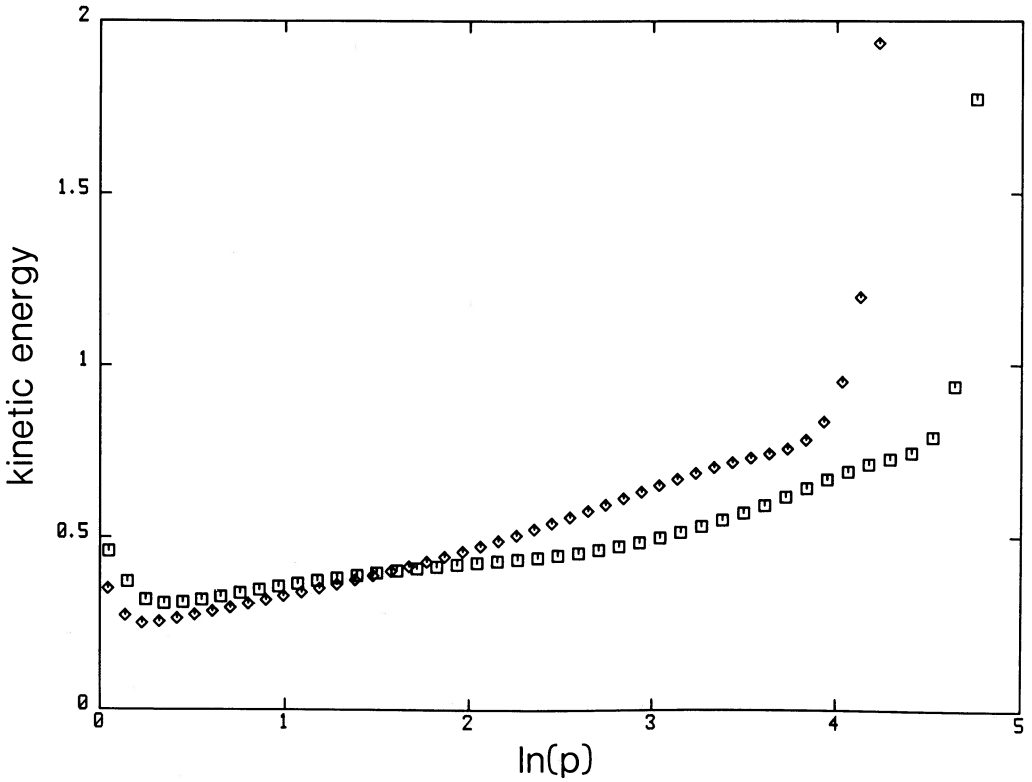

FIG. 17.—Distributions of the kinetic energy for cases D and F. The kinetic energy generally increases with depth (except at the top).

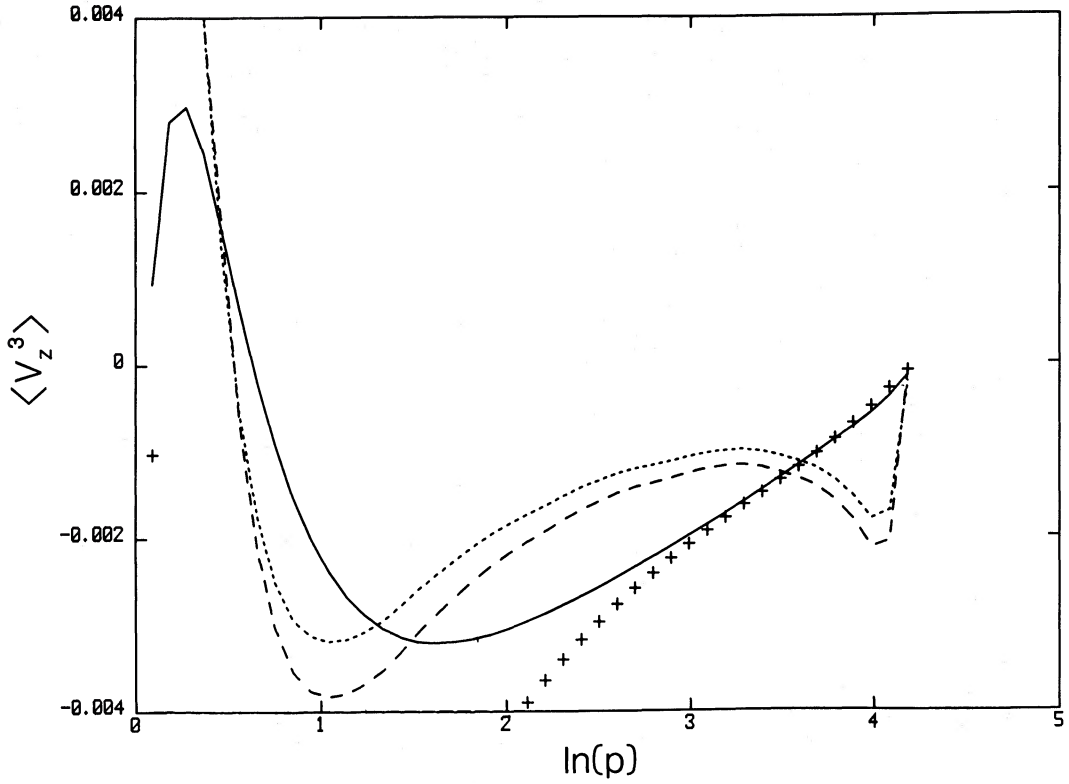

FIG. 18*a*

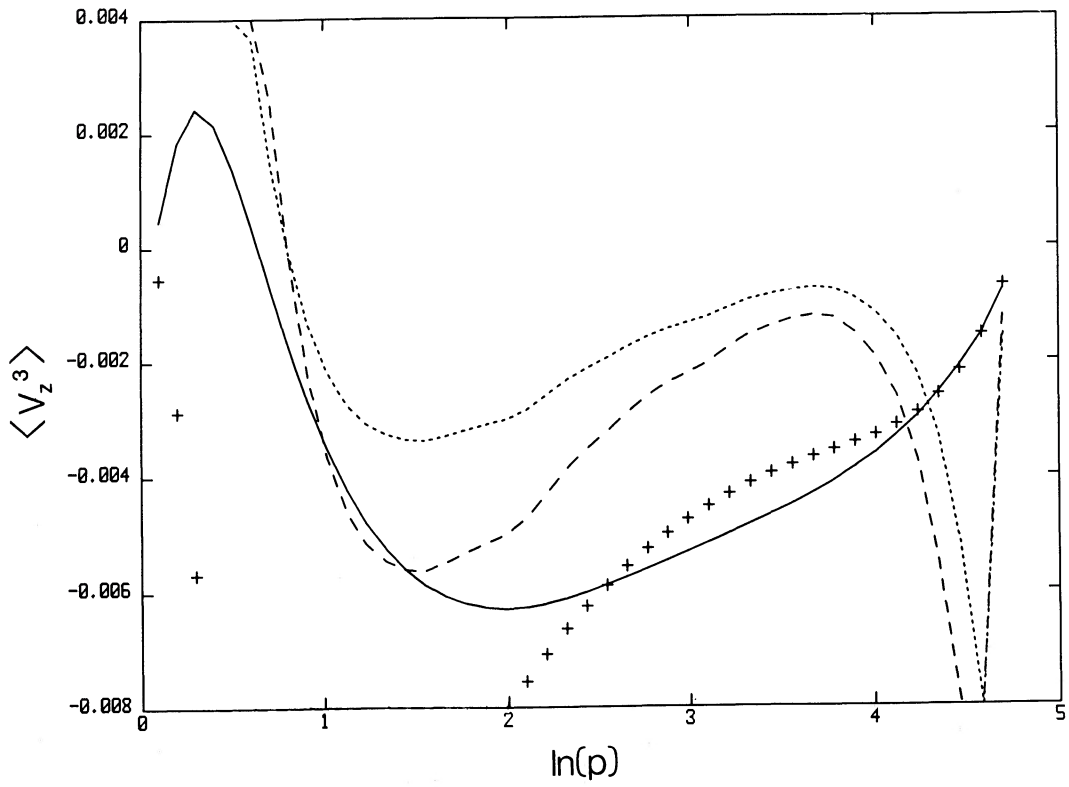

FIG. 18*b*

FIG. 18.—(*a*), (*b*) Comparison of various approximations with the third-order moment of the vertical velocity $\langle V_z^3 \rangle$ (*solid curves*) for cases D and F, respectively. The approximations are $V_z'' \partial V_z''^2/\partial \ln p$ (*dotted curves*), $V_z'' \partial V_z''^2/\partial \ln \rho$ (*dashed curves*), and $-V_z''^3$ (*pluses*).

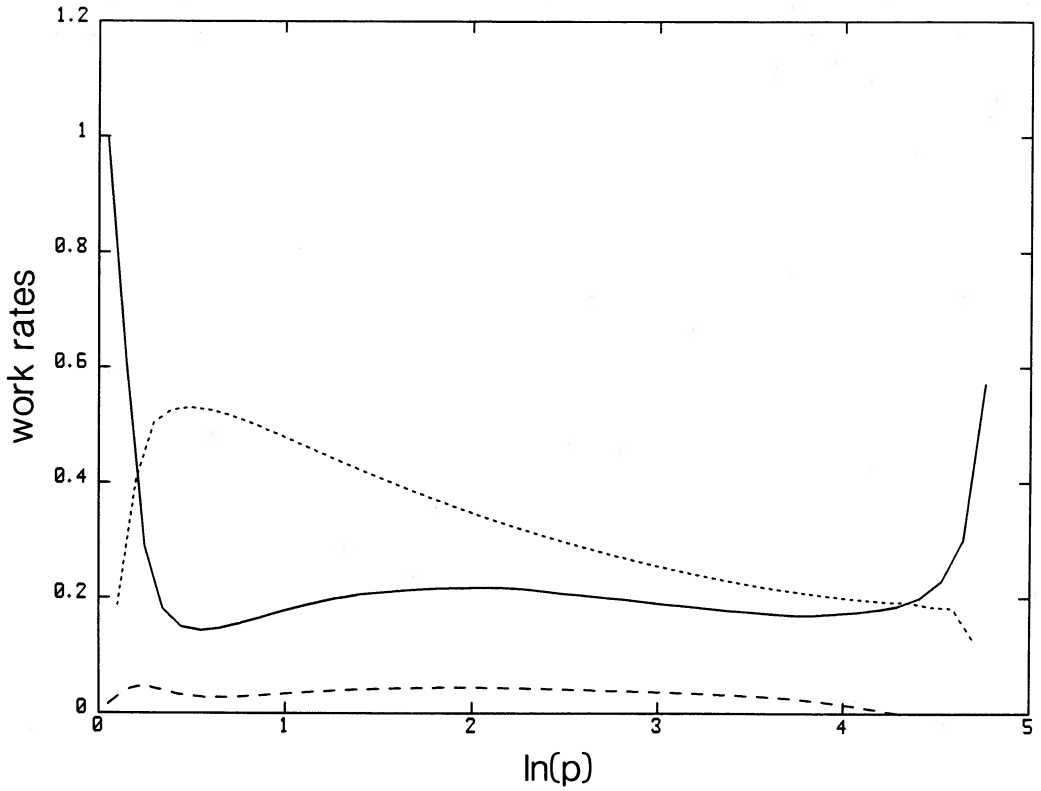

FIG. 19.—Distributions of the rates of buoyancy work (*dotted curve*), dissipation (*solid curve*), and work of the pressure fluctuation (*dashed curve*). The work of the pressure fluctuation is relatively small. In most of the convection zone, the buoyancy work decreases with depth. The dissipation rate peaks near the upper and lower boundaries.

buoyancy work peaks near the top by using relations R15 and R20 to write

$$W_g \approx 0.8(F_{ep}/C_p)(|g|/\langle T\rangle) . \quad (19)$$

Since F_{ep} is only a slowly varying function, W_g is approximately proportional to $1/\langle T\rangle$ and therefore peaks near the top. The distribution of W_v is rather flat in the mid-region but peaks at the upper and lower boundaries where the updrafts and downdrafts are stopped and severe dissipation of kinetic energy occurs.

To proceed further, we now make some very gross approximations in equation (14) to explore the depth dependence of F_k. We ignore all terms except those involving F_k and W_g, and we approximate W_g by equation (19) with the additional replacement of F_{ep} by F_b. Then, we have

$$\partial F_k/\partial z \sim 0.8(F_b/C_p)/H_p , \quad (20)$$

where H_p ($=\langle T\rangle/|g|$) is the pressure scale height. The integral of this equation suggests that $|F_k|$ increases linearly with the number of pressure scale heights and is scaled by the factor F_b/C_p. Does similar behavior hold in actual situations? Figure 20 plots $F_k/(F_b/C_p)$ versus ln p for all cases. Cases with the same γ cluster closely with each other, and therefore the scaling with F_b is very good. Considering the smallness of the difference between the two clusters and the large difference in C_p (2.5 and 6.67), the scaling with C_p is also good. Before effects of the lower boundary set in, the magnitude of F_k also increases with the number of pressure scale heights from the top. With two terms in equation (14) already scaled by F_b/C_p, it is natural to ask whether the other terms are also similarly scaled. Figures 21 and 22 plot $W_v/(F_b/C_p)$ and $W_{p'}/(F_b/C_p)$, respectively, for all the cases. Considering that F_b/C_p varies over a factor of 5, the clustering of the cases in both figures is remarkable. In the mid-region of the convection zone, $W_v/(F_b/C_p)$ is rather uniform and holds values around 3.4 (standard deviation 0.6).

The most serious question concerning F_k is its behavior in deeper convective regions. At the moment, we cannot provide a definite answer to this question, as our numerical cases are not deep enough. There are some arguments that lead us to believe the F_k may be bounded, but they can only be considered as suggestive, since they make use of relations extrapolated to deeper convection zones. First, suppose that W_v stays quite uniform even in deeper layers. Then W_g will eventually drop below W_v according to equation (19), and $|F_k|$ will decrease; W_v will also follow. Second, if $-V_z''^3$ approximates $\langle V_z^3\rangle$ well in the deeper region, as indicated by Figures 18*a* and 18*b*, then, using relations R25, R26, R21 and the approximation $F_{ep} \cong F_b + |F_k|$.

$$|F_k| \sim 0.81(F_b + |F_k|)/C_p . \quad (21)$$

This equation can be solved to obtain

$$|F_k| \sim (F_b/C_p)/(1.2 - 1/C_p) , \quad (22)$$

which is bounded by 1.3 F_b/C_p since C_p is not less than 2.5. For cases A–F, the maximum values of $|F_k|/(F_b/C_p)$ reach 1.13, 1.15, 1.05, 0.96, 1.24, and 1.32, respectively. The depth of our computed cases may be just below what is needed to ascertain the deeper behavior of F_k.

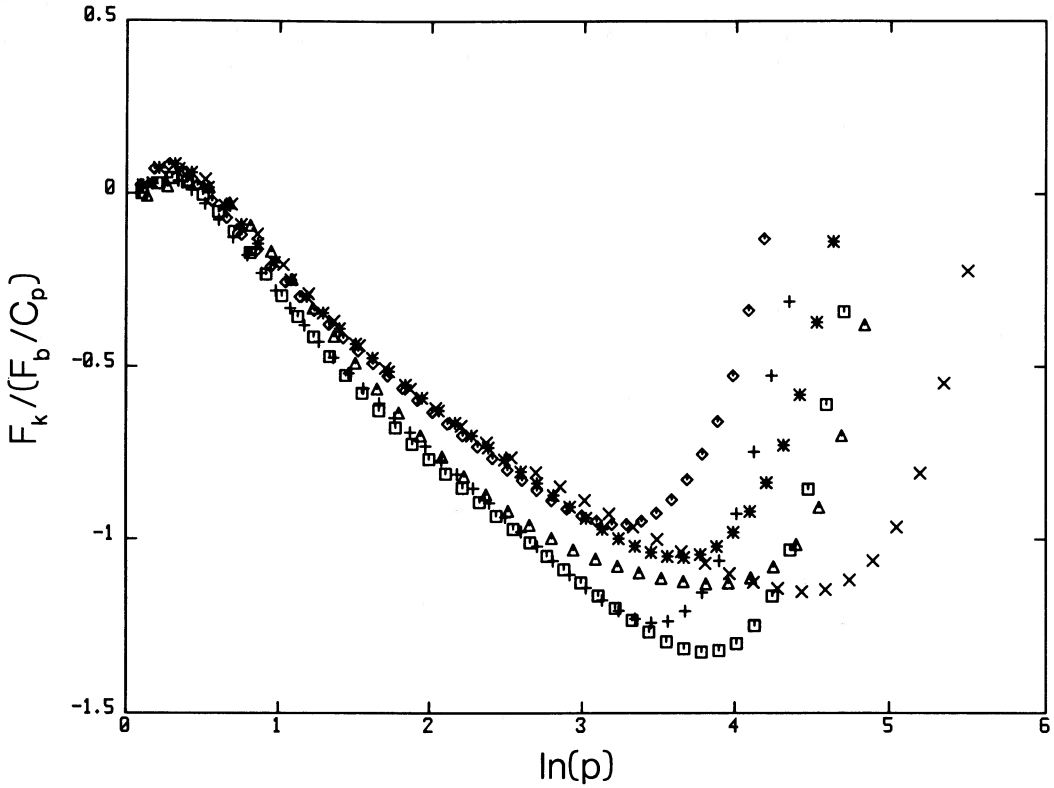

FIG. 20.—Distributions of $F_k/(F_b/C_p)$ for all cases. Aside from the spread near the bottom which is caused by the different depths of the lower boundary for different cases, all the distributions are close to each other. Cases with different γ fall into two slightly different groups.

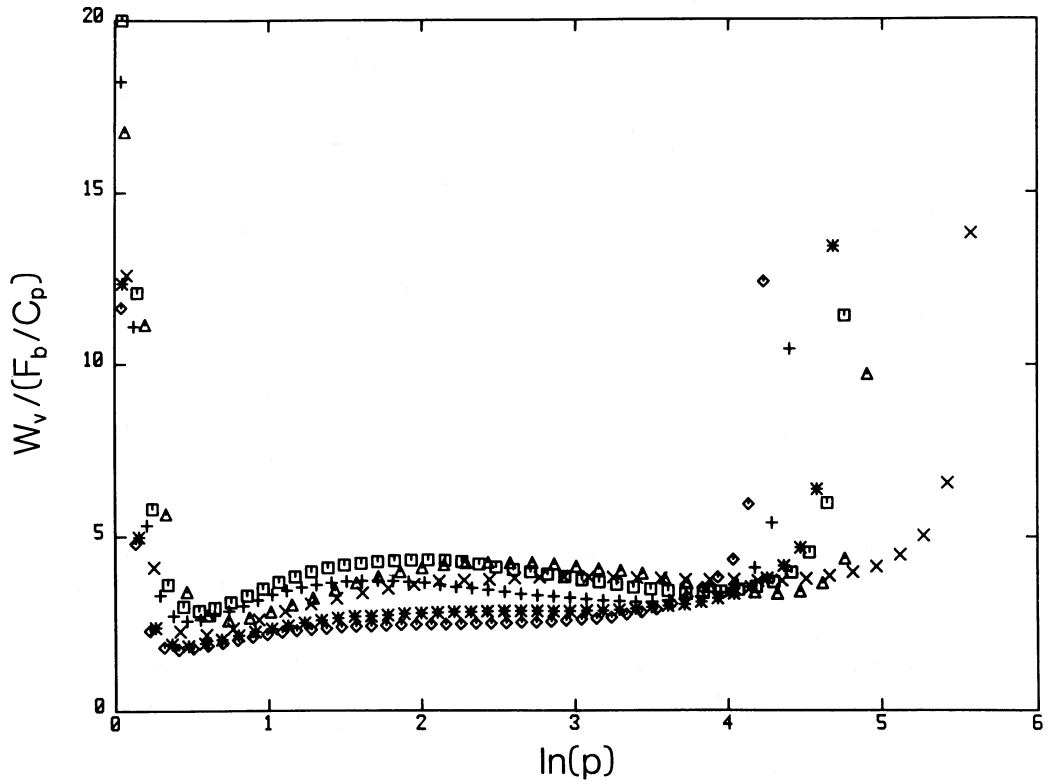

FIG. 21.—Distributions of $W_v/(F_b/C_p)$ for all cases. They roughly overlap with each other and stay quite uniform in the mid-region of the convection zone.

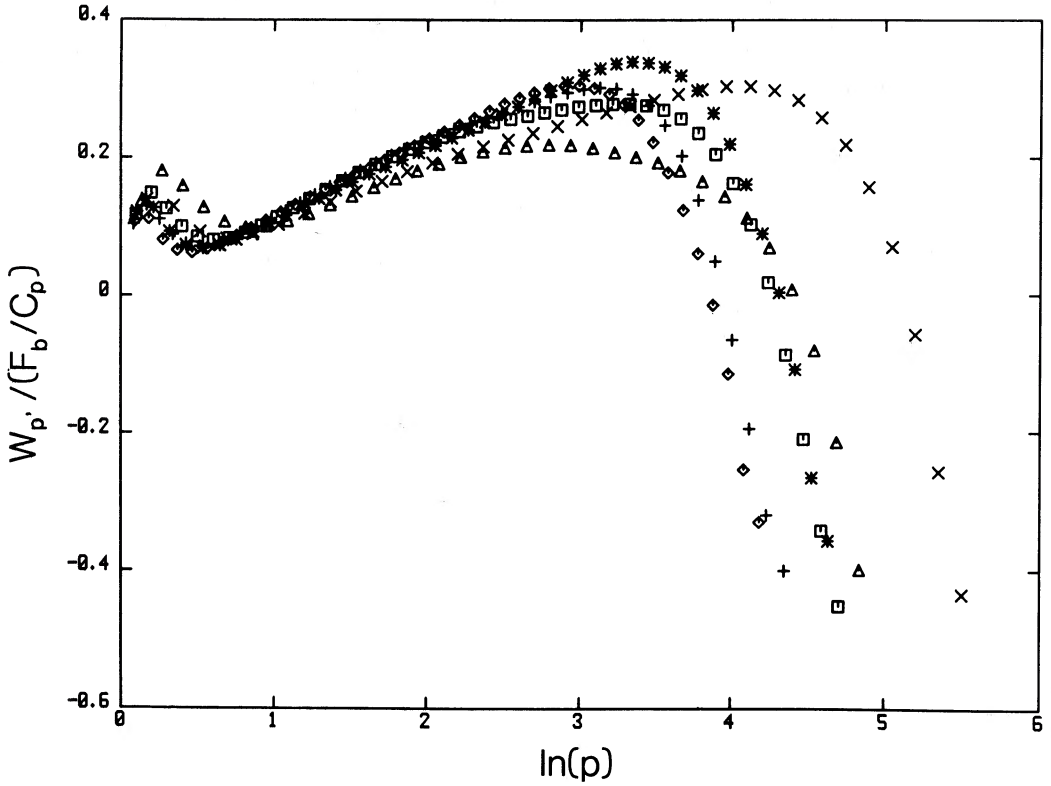

FIG. 22.—Distributions of $W_{p'}/(F_b/C_p)$ for all cases. They also roughly overlap with each other.

V. SUMMARY AND DISCUSSION

In this paper, we compile a collection of approximate formulae that relate the variations and correlations of the deviations induced by the convective turbulence. Some relations are more reliable than others, and some can only be considered as suggestive. All listed relations do not contain g explicitly. In a few occasions (e.g., $C[\rho', T']$) some dependence in γ is indicated, but the variations are usually relatively small so that we chose to ignore the dependence. The two ratios of specific heats adopted by our numerical cases bracket the range of effective γ that can occur in stellar convection zones quite well.

The links among the relations are as follows:

1. When the ratios between the magnitudes of fluctuations of the thermodynamical variables are known, the correlation coefficients between pairs of these variables can be determined.

2. The mean vertical velocity, assumed to be zero from time to time, turns out to be an important quantity that describes the mean advection of thermal variables. In particular, it connects the rate of buoyancy work to the convective flux.

3. Almost all the single-point, second-order correlation functions (rms fluctuations or covariance) of the primitive dynamical variables can be expressed in terms of $\langle V_z \rangle$ (or V_z'').

4. In regions where the superadiabatic gradient is not negligible, say greater than 0.005, $\Delta\nabla$ can be roughly computed from the total flux; the presence of the flux of kinetic energy does not introduce serious error to the estimate.

5. The downward flux of kinetic energy cannot be treated as a diffusive flux of kinetic energy. To treat it as a diffusive flux of mean square velocity is also questionable. It is possible that this flux can be approximated as $(-\frac{1}{2})\langle\rho\rangle V''^3$ in deep regions.

6. The production and dissipation of the kinetic energy do not parallel each other. Production is scaled by the total flux, and the local production rate is only a function of local mean variables. The dissipation is clearly nonlocal; significant amount of kinetic energy is carried away from the production region and is dissipated at the upper and lower boundaries where the flux of kinetic energy is forced to zero.

Probably the local scaling relationships between turbulence and structure hold because they are associated with the production process. Standard arguments of MLT go along this line by considering the acceleration of bubbles, but after the kinetic energy of the bubbles is produced, MLT makes it disappear mysteriously after one mixing length. A more complete picture, given by the numerical computations, is that after production, significant amount of kinetic energy is transferred downward, to be dissipated in lower regions.

The behavior of the flux of kinetic energy in deeper convection zones has not been determined. Further calculations with deeper stratification are needed. The behavior of the dissipation rate of kinetic energy in deeper regions is also unknown. It is necessary to calculate models with a stable layer below the convection zone to determine the natural development of F_k, W_v, $W_{p'}$ and their implication on overshooting.

The relationship between the superadiabatic gradient and the total flux has not been established for transition regions where the superadiabatic gradient is on the order of 0.1 to 1 and the effects of radiative transfer become significant. Models with a radiative layer on top are needed to study such a regime.

This research is partially supported by NSF (AST-8504399). S. S. thanks NASA for support.

REFERENCES

Chan, K. L., and Sofia, S., 1986, *Ap. J.*, **307**, 222 (Paper III).
———. 1987, *Science*, **235**, 465 (CS).
Chan, K. L., Sofia, S., and Wolff, C. L. 1982, *Ap. J.*, **263**, 935.
Cox, J. P., and Giuli, R. T. 1968, *Principles of Stellar Structure* (New York: Gordon & Breach).
Gough, D. O. 1969, *J. Atm. Sci.*, **26**, 448.
Hurlburt, N. E., Toomre, J., and Massaguer, J. M. 1984, *Ap. J.*, **282**, 557.
Massaguer, J. M., and Zahn, J.-P. 1980, *Astr. Ap.*, **87**, 315.
Sofia, S., and Chan, K. L. 1984, *Ap. J.*, **282**, 550.

KWING L. CHAN: Applied Research Corporation, 8201 Corporate Drive, Landover, MD 20785

SABATINO SOFIA: Center for Solar and Space Research, Yale University, New Haven, CT 06511